PHYSICAL REVIEW A VOLUME 45, NUMBER 12 15 JUNE 1992

Molecular-dynamics simulations of two-dimensional materials at high strain rates

Norman J. Wagner,* Brad Lee Holian, and Arthur F. Voter
Los Alamos National Laboratory, Los Alamos, New Mexico 87545

(Received 23 December 1991)

The mechanical behavior of model two-dimensional materials is investigated by large-scale molecular-dynamics (MD) simulations on a massively parallel computer. Both a pair-potential and a model embedded-atom many-body potential are examined. A parallel MD algorithm is developed to exploit the architecture of the Connection Machine, enabling simulations of greater than 10^6 atoms. Adiabatic expansions and spallation experiments on both perfect crystals and granular solids are performed. It is demonstrated that a uniform adiabatic expansion is a good model for the spallation process. The spall strength is shown to be proportional to the logarithm of the applied strain rate. A dislocation-dynamics model is developed to explain the results, which also leads to predictions for the impact spallation experiments.

PACS number(s): 05.70.Ln, 81.40.Lm, 62.50.+p

I. INTRODUCTION

Fracture and failure of simple and complex materials remains a fundamental problem for materials scientists designing new materials, engineers applying materials to specific applications, and investigators intrigued by the mechanisms underlying the phenomena [1]. Recently, more attention has been focused on understanding the molecular mechanisms that give rise to the macroscopic failure process, partly due to the advent of massively parallel computers enabling the simulation of large ensembles of atoms. Unlike many equilibrium material properties that can adequately be represented by suitable simulations of hundreds or thousands of atoms, fracture and failure involve both microscopic and macroscopic length scales. For example, crack propagation or stress concentration near a crack tip inherently depends on both the molecular properties of bonding and atomic arrangement and the macroscopic properties of the crack length and crack-tip geometry. Further, materials with multiple levels of structure, such as polycrystalline or nanocrystalline solids, require large ensembles of atoms to accurately represent these mesoscopic structures. Such considerations have motived the development of a molecular-dynamics (MD) simulation tool on a massively parallel computer for investigating material behavior at the molecular level.

Fracture and failure processes also depend on strain rate. We have chosen to investigate one interesting regime of material failure, namely, spallation at high strain rates. Through the use of molecular-dynamics simulations we hope to elucidate the molecular mechanisms underlying material failure at these extreme conditions. This is motivated by the following two considerations: (i) detailed microscopic analyses are difficult to perform during spallation, and (ii) molecular dynamics is well suited to examining processes that occur on these short-time scales. Simulations can also provide detailed information concerning microscopic mechanisms for spallation at high strain rates, about which little is known [2,3].

In this work, a molecular-dynamics simulation approaching experimentally realizable size and time scales is developed. We apply the technique to a two-dimensional model system, exploring high-strain-rate spallation and examining the molecular mechanisms leading to failure. It is not the goal of this initial work to model actual materials, but rather to study generic material behavior. To this end, both a pure pair-potential material and a many-body potential material, which have been well characterized [4], are examined. A scaled-down version of a typical spallation experiment is simulated as well as a simpler adiabatic expansion test consisting of plane uniaxial strain. Initial investigations of the effects of polycrystallinity are also discussed. The results of these tests are compared against an energy criterion for spallation, and become the basis for a postulated dislocation-dynamics model used to explain the observations.

The paper proceeds by a brief discussion of the computational algorithm and a definition of the interatomic potentials employed. Results for the spallation simulation are then discussed. Adiabatic tensile tests are also presented and analyzed through a theory based on energy balances. The simulation results suggest an empirical model derived through dislocation dynamics, which is used to explain the gross features of the spallation simulations.

II. COMPUTER-SIMULATION TECHNIQUE

To address the physics of shock propagation in metals, a molecular-dynamics computation algorithm has been developed for the massively parallel SIMD Connection Machine (CM-2). The atoms follow Newton's equations of motion, which are simply integrated forward in time via a half-step Stoermer algorithm [5]. Given that our potentials (including the many-body potential) can be cast in a pairwise additive form, it is advantageous to move particles through a Eulerian grid. The spatially periodic simulation cell is divided into n_x by n_y boxes of dimensions δx by δy. When these box lengths are greater than or equal to the range of the interaction potential, searching a particle's eight neighboring boxes plus its own box produces the required sum over neighboring particles. This avoids a linked neighbor list and enables complete parallelization of the time-consuming calculations. All the arrays have an additional dimension of pigeonholes, so that more than one particle can occupy the same Eulerian box in space.

The particles move according to Newton's equations of motion (in time-discretized form)

$$\mathbf{X}_t=\mathbf{X}_{t-1}+\mathbf{U}_{t-(1/2)}\Delta t \;, \tag{1}$$

$$\mathbf{U}_{t+(1/2)}=\mathbf{U}_{t-(1/2)}+\mathbf{F}_t\Delta t \;, \tag{2}$$

where the positions $\mathbf{X}$, velocities $\mathbf{U}$, and forces $\mathbf{F}$ are evaluated for each particle in parallel and the necessary storage of data is minimized.

The interatomic forces are treated as central forces, modeled as a combination of a Lennard-Jones (LJ) 6-12 with a spline cutoff and an analytic embedded-atom many-body potential, as detailed previously [4]. This many-body potential has been successfully employed as a model for ductile metals. The total potential can be written as

$$\Phi=\sum_{i=1}^{N}\left[\frac{1}{2}\sum_{i\neq j}\varphi(r_{ij})+F(\rho_i)\right] , \tag{3}$$

where r_{ij} is the center-to-center separation distance and ρ_i is the local density. The LJ 6-12 part has the cutoff form

$$\varphi_{\mathrm{LJ}}(r)=\begin{cases} 4\chi\varepsilon\left[\left[\dfrac{\sigma}{r}\right]^{12}-\left[\dfrac{\sigma}{r}\right]^{6}\right], & r<r_{\mathrm{spl}} \quad (4)\\ -a_2(r_{\max}^2-r^2)^2+a_3(r_{\max}^2-r^2)^3 , & r_{\mathrm{spl}}<r<r_{\max} \quad (5)\end{cases}$$

where ε is the LJ well depth, χ is a weighting parameter between zero and 1, σ is where the LJ potential goes through zero, r_{spl} is the inflection point in the potential, and

$$r_{\max}^2=r_{\mathrm{spl}}^2\left\{5-5\left[1-\frac{1}{25}\left[9-\frac{24\varphi(r_{\mathrm{spl}})}{r_{\mathrm{spl}}\varphi'(r_{\mathrm{spl}})}\right]\right]^{1/2}\right\} , \tag{6}$$

$$a_2=\frac{5r_{\mathrm{spl}}^2-r_{\max}^2}{8r_{\mathrm{spl}}^3(r_{\max}^2-r_{\mathrm{spl}}^2)}\varphi'(r_{\mathrm{spl}}) , \tag{7}$$

$$a_3=\frac{3r_{\mathrm{spl}}^2-r_{\max}^2}{12r_{\mathrm{spl}}^3(r_{\max}^2-r_{\mathrm{spl}}^2)^2}\varphi'(r_{\mathrm{spl}}) . \tag{8}$$

This spline fit does not require taking a square root in the calculation.

The many-body embedded-atom (EAM) term has the analytic representation

$$F[\rho_i]=\tfrac{1}{2}d(d+1)\varepsilon(1-\chi)e\rho_i\ln\rho_i, \quad r<r_{\max} \tag{9}$$

where d is the dimensionality and the local density has the form

$$\rho_i=\sum_{j(\neq i)}w(r_{ij}) , \qquad w(r)=\frac{1}{d(d+1)}\left[\frac{r_{\max}^2-r^2}{r_{\max}^2-r_0^2}\right]^2, \quad r<r_{\max} \tag{10}$$

with $r_0=2^{1/6}\sigma$. The parameter value $\chi=\frac{1}{3}$ was taken for the EAM, while $\chi=1$ returns the pure LJ material.

As discussed previously [4], these two model potentials can be used to represent either "brittle" (LJ) or "ductile" (EAM) materials. Qualitative differences were observed in the plastic flow behavior as the energy required for vacancy formation is a significantly lower fraction of the cohesive energy for the EAM potential. Further, the many-body potential was necessary to properly represent experiments where surfaces and ductility were important.

The computational algorithm loop followed for each microstep Δt is as follows.

(i) Take a step in time, move the particles based on their half-step velocities.

(ii) Locate particles in their proper Eulerian boxes.

(iii) Condense the position arrays to the minimum pigeonholes required.

(iv) Compute the pair-potential contribution to the forces and the "local density" for embedded-atom potential [Eq. (10)] by searching local and neighboring boxes.

(v) Compute the contribution of the embedding function to the forces by searching boxes.

(vi) Calculate new velocities.

(vii) Compute bulk properties.

Each step in the above sequence of operations is completely parallel, since the calculations for each box and the nearest-neighbor communications are handled by all processors in lockstep. The sampling of neighboring boxes on the spatial grid is accomplished by replicating the data structure and shifting this replicate through a spiral sequence of circular shift operations. The extension of this algorithm to three dimensions is straightforward.

There are three time scales in the program: the basic microstep outlined above, a mesoscale step for which box-averaged quantities are reported, and a macrostep for which atomistic quantities are stored. On the mesoscopic time scale, quantities such as local temperature, pressure, stress, and grain orientation can be averaged over all pigeonholes for each Eulerian box, providing a coarse-grained output analogous to that obtained from a typical continuum code.

With the above algorithm, there are various optimizations that can reduce computation time. For the problem studied here, there are large fluctuations in density due to shock waves. Hence, eight pigeonholes were required, although only three on average were filled with actual particles. The effective speed of the code is slowed down by the many vacant pigeonholes that are carried through the calculations. Condensing to the minimum required at each time step before the force loop increased the efficiency. The program, written in FORTRAN 90, was run on the 64K-processor CM-2 (see Acknowledgments).

The computational time on the CM for a configuration of 512×512 ($n_x\times n_y$) boxes with eight pigeonholes per box required 5 s per microstep. The EAM potential, which requires computation of the local density, takes roughly twice as long for the computation of forces as the LJ pair potential. We believe this algorithm efficiently exploits the state-of-the-art architecture of the CM-2 such that it is approximately ten times faster than the equivalent code on the Cray Y-MP (single processor) and can be expanded to over 20 times the total number of atoms (i.e., 8 million). Thus, parallel computation enables studies of nearly macroscopic ensembles of atoms on time scales appropriate to high-strain-rate experiments, such as shock waves and spallation.

III. SIMULATION RESULTS

A. Spallation experiments

A plane-wave impact experiment was simulated to investigate the molecular aspects of spallation. In this experiment, translational momentum is converted into irreversible work consisting of heat and defect generation. The elastic and elastoplastic solutions for the wave propagation and shock formation are well known and lead to good agreement with experiments [6,7]. For relative impact velocities exceeding about 10% of the sound velocity, most solids are observed to deform plastically. For perfect crystals, higher velocities are required in MD simulations to achieve plastic flow [8]. Typically, the majority of the plastic work is converted into heat, with the balance going into defect formation. At high enough impact velocities, rarefaction waves from the free surfaces superimpose, leading to spallation. It is the regime near the onset of spallation that we wish to investigate at the molecular level.

We simulated materials with interaction potentials as described above. The experimental geometry (Fig. 1) consisted of a flyer plate of mass M moving with x velocity $2v$, that impacts a target plate of mass $2M$ moving with x velocity $-v$, fixing to zero the center-of-mass motion. The total number of atoms in the simulations was $N\approx25\,000$ (requiring $n_x=256$, $n_y=64$). Periodic boundary conditions were used for the y direction, while in the x direction enough free space was allowed around both plates so that no communication occurred across the x boundary during the simulation. The plates were cut from a lattice and equilibrated before the start of the experiment, allowing the free surfaces to relax. Both single-crystal and polycrystalline samples were simulated, as detailed in Table I. The plate velocity relative to the target was chosen to be 1.2 $(\sqrt{\varepsilon/m})$, such that the ratio of particle velocity to sound velocity U_p/c_0 was 0.12 for the EAM material ($c_0\approx5$) and 0.067 for the LJ material ($c_0\approx9$), both in the range where the elastic material response dominated the shock propagation in previous work [6].

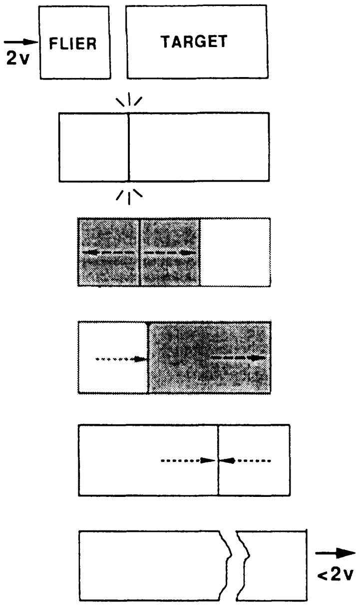

FIG. 1. Spallation experiment geometry.

Upon impact, the plates cold weld together and shock waves propagate outward from the impact point. These waves reflect off the free surfaces, returning as a family of release waves that broaden due to nonlinear effects. Assuming constant wave velocities, these release waves meet at a plane whose distance from the right side of the target is equal to the flyer plate thickness. For strong enough impact velocities, the material fails under this resultant tensile stress and spallation occurs.

Snapshots of initial and final steps in the above sequence are displayed in Fig. 2 for the embedded-atom potential under the conditions listed in Table I under run A. Here, the local density is computed for each box, the crosshatching represents bulk material about the normal density, and the black represents vacuum. The first picture is immediately before impact, where local-density fluctuations due to thermal motion appear as transient darker spots. The second frame shows the state of the

TABLE I. Spallation experiments.

Code	T_{therm} $(t=0)$	T_{shock} $(t=0)$	Potential	U_p/c_0	Polycryst.	Spallation	ΔW_{irr}[a]
A	0.17	0.16	EAM	0.24	No	Yes	23%
B	0.17	0.16	LJ	0.13	No	No	22%
C	0.075	0.16	EAM	0.24	No	Yes	23%
D	0.17	0.16	EAM	0.24	Yes	Yes	23%

[a] ΔW_{irr} represents the loss in total kinetic energy to irreversible work minus heat generation.

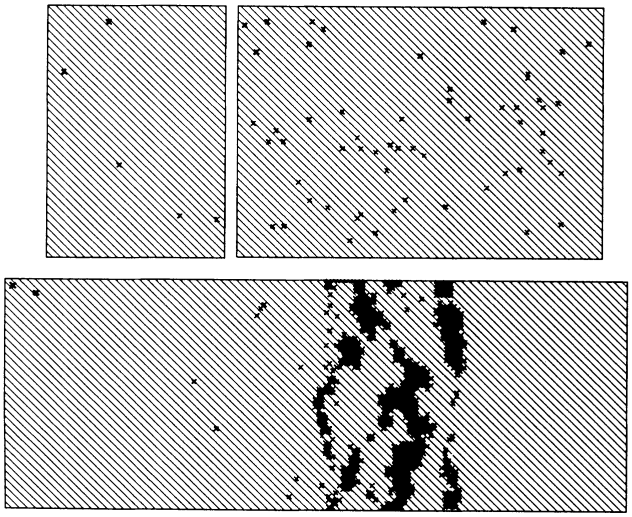

FIG. 2. Spall run A (EAM model material), showing the initial flyer and target plates (a) initially and (b) after spallation.

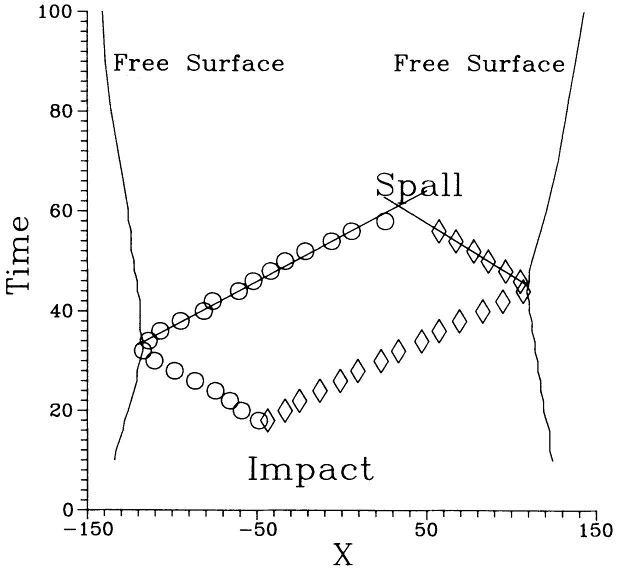

FIG. 3. Spall run A position-time plot of the shock wave fronts and plate free surfaces.

material during spallation, where there is almost perfect welding at the impact plane, as expected for a material free of contaminants. The release waves have since crossed, and large voids and cracks have opened up perpendicular to the strain at the spall plane. The target material has failed and the spalled material is moving off to the right, eventually separating with some fraction of the initial kinetic energy. As is more evident from a movie, the spallation proceeds by the opening up of small voids, which eventually coalesce into long cracks normal to the impact direction. The material between neighboring cracks undergoes strong plastic flow and yields, many times necking down to bridges of single atoms before separation.

As expected, the shock front velocity and the location of the spall plane can be readily predicted from simple one-dimensional hydrodynamics. From the plane of impact, planar shock wave fronts propagate at the shock velocity back into the colliding material until meeting the free surfaces. The shock waves reflect and then propagate back through the compressed material as self-similar release waves until they meet, defining the spall plane. A time-position plot corresponding to the pictures is shown in Fig. 3. As the self-similar release waves propagate, their front positions broaden and become ambiguous.

In Fig. 4 some typical plots of x-velocity profiles through the sample before and during spallation are shown. Initially, the two plates are freely flying toward one another, each with a uniform velocity. These curves are obtained by averaging over all the particles in the pigeonholes and then over all the boxes in the y direction, yielding the average x velocity of all particles in a column within $x \rightarrow x+\delta x$, where δx is the width of the computation box (equal to or greater than the potential cutoff distance). Initially the shock fronts are very sharp, spanning only one or two boxes. For the perfect crystals, it was observed that the shock fronts were also planar. However, in the polycrystalline experiments, although the shock fronts were also sharp, the front was not as planar due to the propagating wave encountering nonhomogeneous distributions of grain boundaries. This leads to a slight smearing of the front velocities on these averaged plots. The second curve shows the state of the x velocity some time after the tensile waves have met ($t=41t_0$, $t_0=\sigma\sqrt{m/\varepsilon}$). It is interesting to see that the tensile waves have combined to form an almost linear, tensile-strain field across the spall plane. This occurs on a relatively short time scale, so that the process strongly resembles an adiabatic expansion under plane strain, a point discussed in some detail below.

Some macroscopic details of the spallation process provide a quantitative measure of where the initial kinetic energy ends up after spallation. Figures 5(a) and 5(b) show plots of various kinetic energies during the simulation. The temperature defined in terms of the average kinetic energy per particle is

$$T_{\text{tot}}=\frac{m}{2Nk_B}\sum_{i=1}^{N}[(U_i-U_{\text{c.m.}})^2+V_i^2]\ , \tag{11}$$

where U and V are the x and y velocities, respectively, and the subscript c.m. denotes the center-of-mass velocities, which are zero in our reference frame. The local thermal temperature is defined as

$$T_{\text{therm}}=\frac{m}{2Nk_B}\sum_{i=1}^{N}[(U_i-\overline{U}_i)^2+V_i^2]\ , \tag{12}$$

where the overbar indicates the average over all n_y boxes in the same x slice as particle i, as described above. By subtracting off the local x velocity due to the imparted motion, T_{therm} approaches the thermodynamic temperature. Similarly, the shock contribution to the effective temperature can be defined as

$$T_{\text{shock}}=\frac{m}{2Nk_B}\sum_{i=1}^{N}(\overline{U}_i)^2 \ . \tag{13}$$

This initially equals $\frac{1}{2}$ of the initial imposed kinetic energy by the bulk plate motion. As shown in Fig. 5(a) for the EAM material, the thermal and translational contributions to the kinetic energy are roughly equal at time zero. After impact ($t\approx 15$), the shock energy is converted into thermal energy and the total kinetic energy drops as some is stored in potential energy. The curves show a change in slope as the left-moving shock wave hits the back of the flyer ($t\approx 30$) and then a turn as the right-moving shock wave reflects off the back of the target plate ($t\approx 45$), signifying the end of shock compression. For a perfectly elastic material, these energies should simply return to their original value, but do not because there is significant kinetic-energy dissipation during the spallation process. Further kinetic energy is lost as the material yields and the back of the target plate separates, taking with it a significant fraction of the original kinetic energy ($\approx$40%). In this example, the difference between the initial shock kinetic energy and the final kinetic energy due to bulk motion is dissipated as a small increase in thermal temperature and additional irreversible work done in spallation. This work, representing both the plastic flow and the creation of new surfaces, cracks, and voids in the sample, totals 23% of the sum of the initial kinetic energy of the sample (thermal plus shock).

For the LJ material under the same conditions, a different behavior is observed. Although the LJ material has the same cohesive energy, its cold sound velocity is

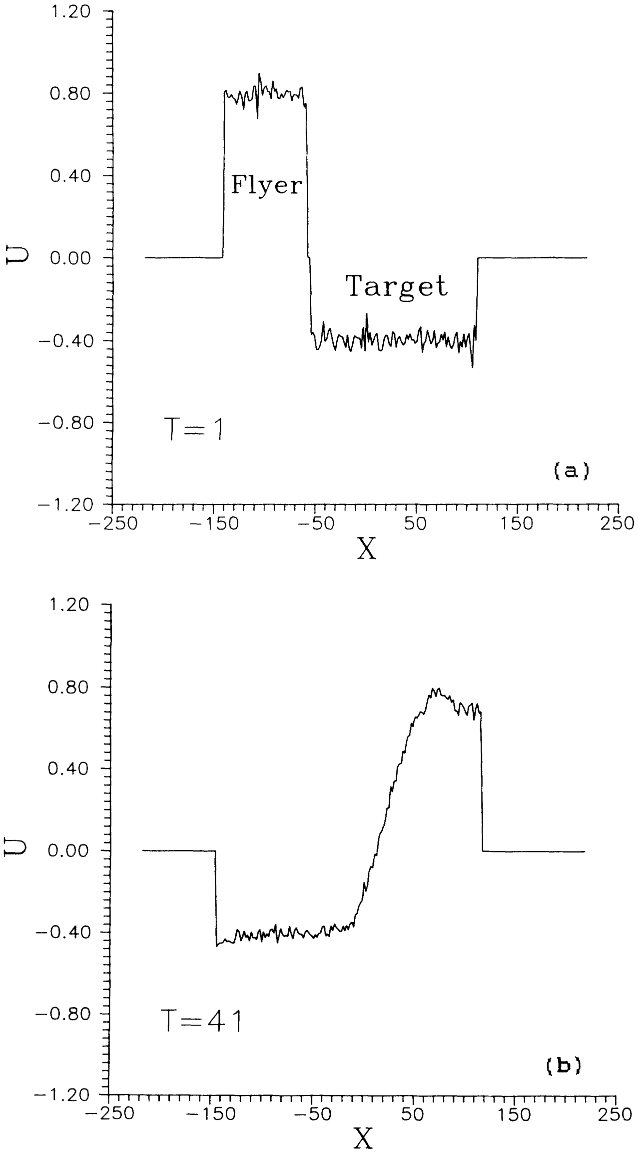

FIG. 4. Run B x velocity as a function of x position for times (a) 1 and (b) 41.

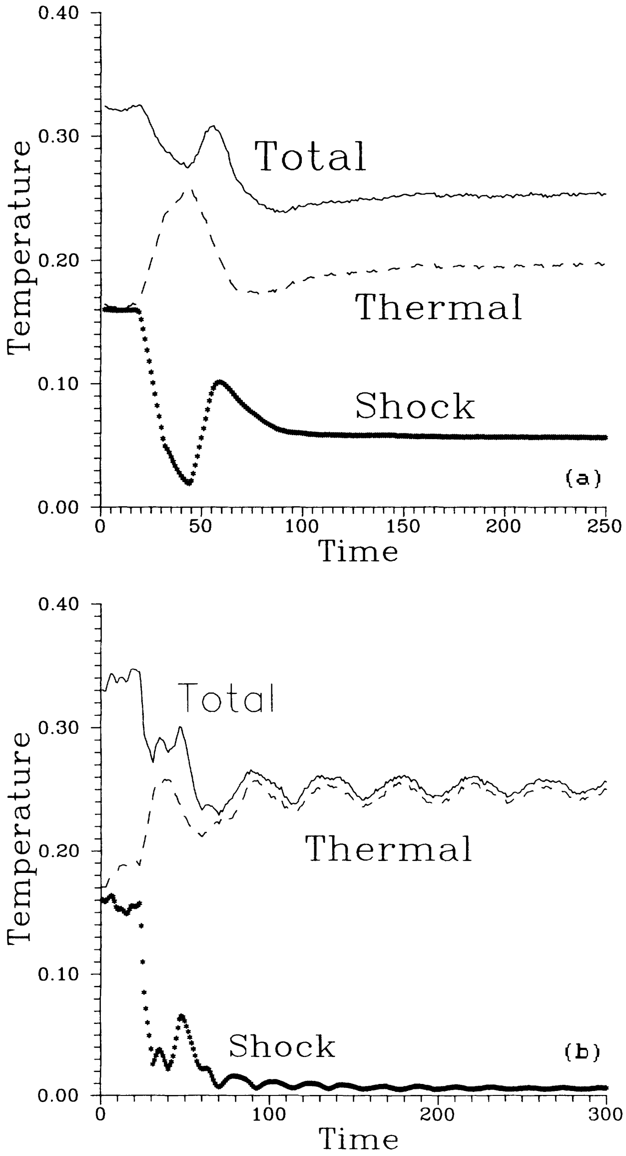

FIG. 5. Kinetic energy vs time for (a) spall run A and (b) spall run B.

almost twice that of the EAM material [4]. Further, the melting temperature is almost twice that of the EAM potential [4]. Thus, for the same choice of initial velocity, temperature, pressure, and sample size, different behavior is expected. As seen in Fig. 5(b), after the release waves cross ($t_0 \approx 40$), significant kinetic energy is dissipated into thermal energy and irreversible damage to the sample. The waves continue to resonate, slowly damping in amplitude. This oscillatory behavior reflects the continued compression and expansion of the material as the two waves, which are out of phase, transverse the material. The damage is not sufficient to totally spall the material. However, damage is done over a wide range around the spall plane as small voids open under tension. All of the initial shock energy is eventually dissipated and there is a more noticeable rise in the thermal energy than was seen in the previous experiment. However, the net loss in the total kinetic energy is almost equal to that in the EAM example above. Table I summarizes all four experiments, showing that this holds for all of the cases studied.

Varying the initial temperature was found to have little effect at these impact velocities, as seen by comparing run A with run C. This is expected, since the mechanical properties are only weakly temperature dependent. Also, comparing runs C and B, where the ratio of temperature to melting temperature is almost equal for the two different materials, demonstrates that the spallation effect is much more sensitive to the nature of the interparticle interactions. As will be shown, the difference in the response of the two materials is governed more by the large variation in the bulk modulus; the LJ material is much stiffer than the EAM material, and is thus better able to sustain a given applied tensile stress.

Polycrystallinity also has an effect. In run D both flyer and target plate were cut out of a block of EAM material that had been melted and cooled, resulting in a polycrystalline sample with crystals of about 100–1000 atoms each. Further annealing was performed to relax the free surfaces. The material appeared stable and showed little or no grain growth on the time scale of the spallation runs. Although the bulk material behavior was comparable to the perfect crystal sample (run A), there were noticeable microscopic differences. The cold weld at the impact plane was less homogeneous and some crystal rearrangement occurred there as the first tensile wave passed through. The spalled samples were qualitatively similar except that small void nucleation points were also observed to open along grain boundaries. The grain sizes here are small enough that intragranular fracture energy should not differ substantially from that required for intergranular fracture, so these results may correspond in some way to experiments on nanocrystalline materials. This phenomenon is of great interest and will be investigated further, requiring larger ensembles to study the effects of granularity. Previous experimental results on spallation in copper samples has been interpreted as a "pseudobrittle" mode of spallation qualitatively similar to what we observed [9]. On one initial test we did not anneal the surfaces of a polycrystalline sample before impact, so that grains on the weld plane were much smaller than those in the interior. As the first tensile wave passed through this region, significant damage, i.e., large voids, drained most of the energy from this tensile wave. The resulting damage at the spall plane was thereby lessened. This qualitative observation is suggestive of a mechanism whereby defects due to grain boundaries could diffuse the sharpness of the tensile shocks in the material, thus reducing the energy available at the spall plane for failure.

B. Adiabatic tensile tests

To help analyze the spall simulations, the longitudinal yield stress of the materials was measured. For these tests an adiabatic plane strain was imposed on a periodic two-dimensional (2D) sample at the same initial density, temperature, and pressure observed in the spall study. The stable material is suddenly subjected to a uniform strain rate in a range encompassing the rates observed in the spall calculations. The periodic cell is then expanded in the horizontal direction with constant boundary velocity [10]. This corresponds to initial energy input as opposed to a continuous acceleration of the material. The Eulerian strain rate is then a function of time

$$\dot{\epsilon}_{xx}(t)=\frac{\dot{\epsilon}_{xx}(0)}{1+\dot{\epsilon}_{xx}(0)t} . \qquad (14)$$

In this work no dependencies on computational parameters such as the number of atoms and the time step Δt were observed, ensuring that the results are a fundamental property of our two-dimensional materials.

A periodic triangular solid with a specified temperature and density were constructed and adiabatically strained, as described. The studies show that the material has exceptional modulus, as expected for a perfect crystal without defects. The elastic moduli of both the EAM and LJ potential materials were measured by the

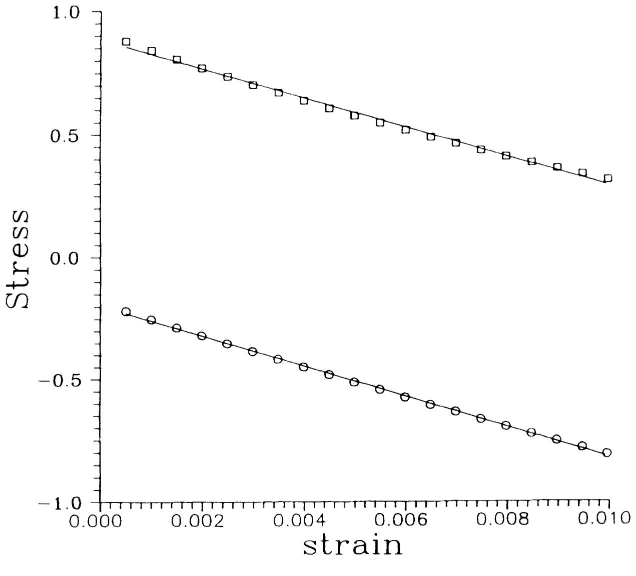

FIG. 6. P_{xx} vs strain for the LJ model at $\dot{\epsilon}=1.0$. ○, $\rho_0=0.916$; □, $\rho_0=0.910$.

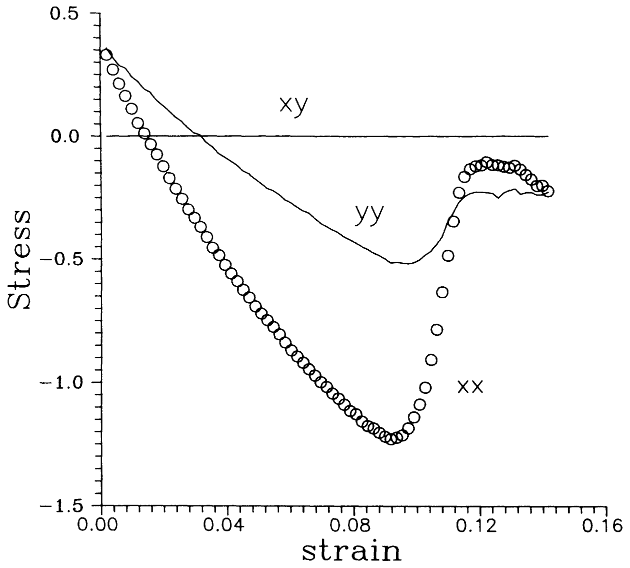

FIG. 7. Pressure tensor components vs strain for the EAM material at $\dot{\epsilon}_0 = 10^{-3}$, $T = 0.17$.

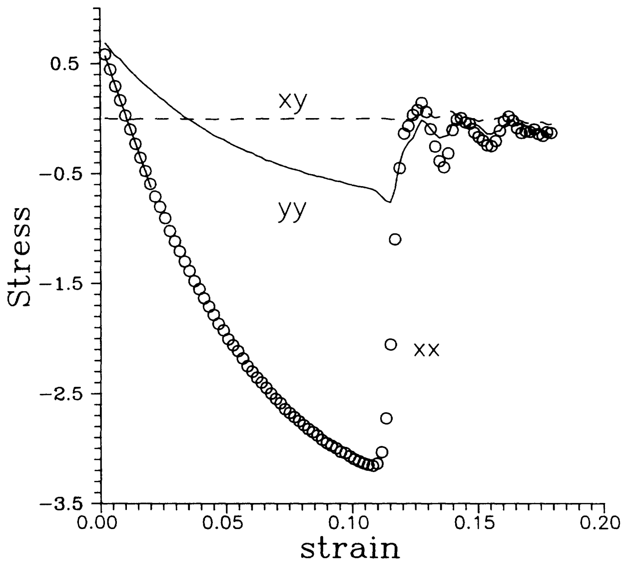

FIG. 8. Pressure tensor components vs strain for the LJ material at $\dot{\epsilon}_0 = 10^{-3}$, $T = 0.17$.

following method appropriate for two-dimensional triangular lattices. For our test geometry with free surfaces in the expansion direction and periodic boundary conditions in the orthogonal direction, the components of the two-dimensional stress tensor σ_{ij} in terms of the strain tensor ϵ_{ij} for plane strain (no Poisson's contraction) are

$$\begin{aligned} \sigma_{xx} &= (B+G)\epsilon_{xx} , \\ \sigma_{xy} &= \sigma_{yx} = 0 , \\ \sigma_{yy} &= (B-G)\epsilon_{xx} , \end{aligned} \tag{15}$$

where B and G are the bulk and shear moduli, respectively. Given the measurements of the stress tensor versus strain, it was straightforward to get the two moduli in the linear limit, and from this, all of the equivalent material properties. A typical example, demonstrating the regime of linear elastic behavior out to 1% strain, is shown in Fig. 6. All of the simulations used here were done at $T = 0.17$ using approximately 16 000 atoms. The values determined for the 2D Young's modulus E (in units of ε/σ^2) and Poison's ratio ν are reported in Table II.

Figure 7 shows the full form of the stress versus strain curve for the EAM material at low initial strain rates (as compared to the atomic vibrational frequency). As seen, the material fails catastrophically but the stresses do not go to zero. Rather, there is some necking of the material between voids so it maintains a small stress However, at high expansion rates, the material yields as the atoms are pulled out of their potential wells. The atoms relax on a time scale given by the Einstein vibration period, which is nearly equal to the unit of time $t_0 = \sigma\sqrt{m/\varepsilon}$. At lower strain rates the material has time to relax and flow, initiating internal fracture and "premature" failure.

Changing to the LJ pair potential changes a number of factors simultaneously. As stated, the cohesive energy is kept constant for comparison. As shown in Fig. 8, the tensile strength is about $\frac{9}{5}$ that of the EAM material with similar maximum extension. Here, however, the material completely fails, generating release waves that resonate in the sample. A composite plot of the stresses is shown in Fig. 9, covering a wide range in initial strain rates. The material fails catastrophically at the lower shear rates (which are still extremely large when compared to laboratory experiments) but simply pulls apart affinely at high strain rates. This is illustrated in Fig. 10, where the ma-

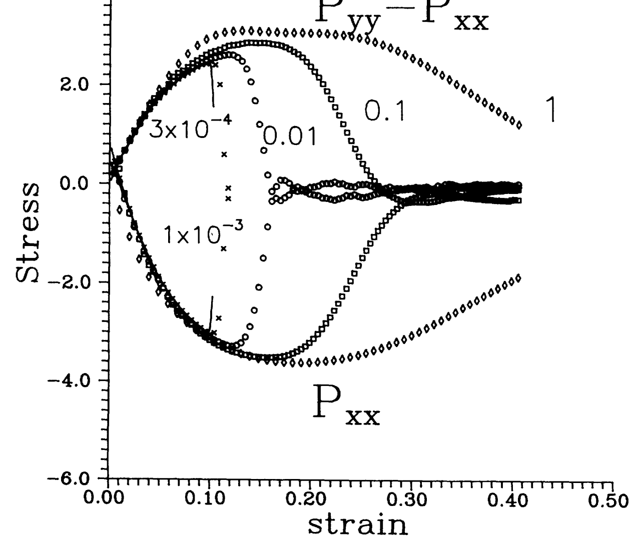

FIG. 9. Pressure tensor components P_{xx} (lower curves) and $P_{yy} - P_{xx}$ (upper curves) vs strain for the LJ material ($T = 0.17$) at $\dot{\epsilon}_0 = 1.0$, 0.1, 0.01, 10^{-3}, and 3×10^{-4} in order, right to left, as labeled.

TABLE II. Spall strength estimates.

Potential	ρ	c_0	E	ν	P^{th}	P^B	P^D
EAM	0.916	5	20	0.49	2.8	$6.9\dot{\epsilon}^{1/3}$	1.4
LJ	0.91	9	57	0.30	5.0	$12.\dot{\epsilon}^{1/3}$	4.5

terial near the failure point is compared for varying strain rates. The general sequence involves a homogeneous nucleation, followed by stress relief waves, void agglomeration, and material failure. The fastest strain rates, corresponding to the atomic vibration time, do not allow for much atomic motion so only a few voids are nucleated before the material fails. Lowering the strain rate results in a longer time before failure, such that the agglomeration of voids into cell-spanning cracks can occur before the material is affinely vaporized. In the strain plots, this is evidenced as failure at a lower total strain. (Also shown in Fig. 10 is a representative result for the EAM potential, where it is observed that the defects resemble voids rather than the cracklike shapes characteristic of the LJ potential.)

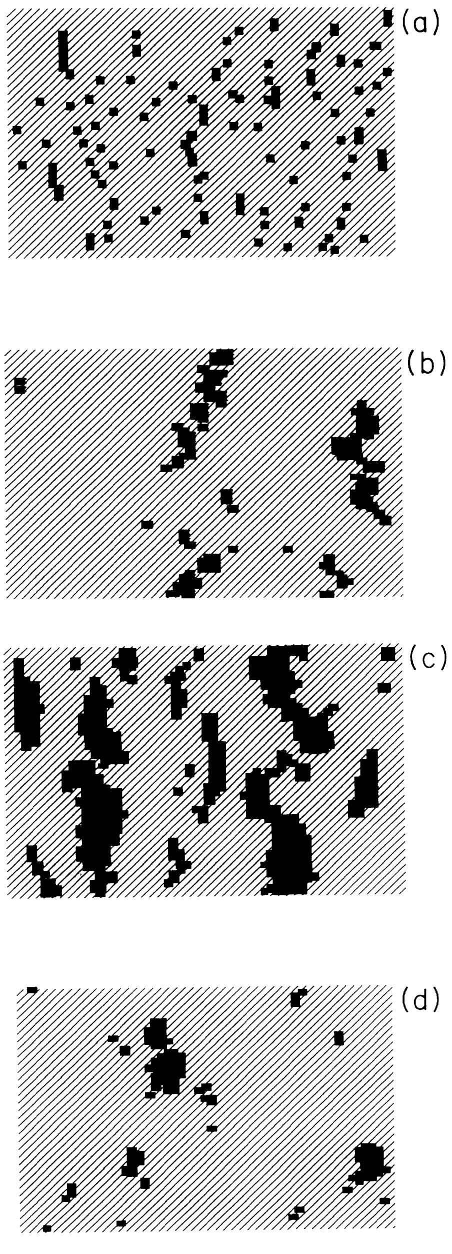

FIG. 10. Adiabatic expansion pictures as a function of strain rate ($T=0.17$). (a) LJ, $\dot{\epsilon}=1.0$; (b) LJ, $\dot{\epsilon}=10^{-3}$; (c) LJ, $\dot{\epsilon}=3\times10^{-4}$; (d) EAM, $\dot{\epsilon}=0.01$.

For the LJ potential, the pressure for an affine deformation of a triangular lattice was computed. Figure 11 shows the results for plane strain of the two orientations of the lattices and for affine dilation. The calculated pressure minimum $[(\sigma_{xx}+\sigma_{xx})/2]$ is very close to that observed in Fig. 8 for $\dot{\epsilon}=1$, in both magnitude and total strain. Thus, this experiment represents the theoretical *dynamic* strength of the material and should be an upper bound for our adiabatic expansion experiments on perfect lattices.

IV. ANALYSIS

A. Energy criterion for tensile test failure

Recent analysis by Grady [11,12] provides an estimate of the spall strength of materials based on a balance between energy storage and the energy required to spall. Three fundamental mechanisms of spall are identified: exceeding the theoretical material strength, brittle fracture, and ductile flow. Below we outline the major argu-

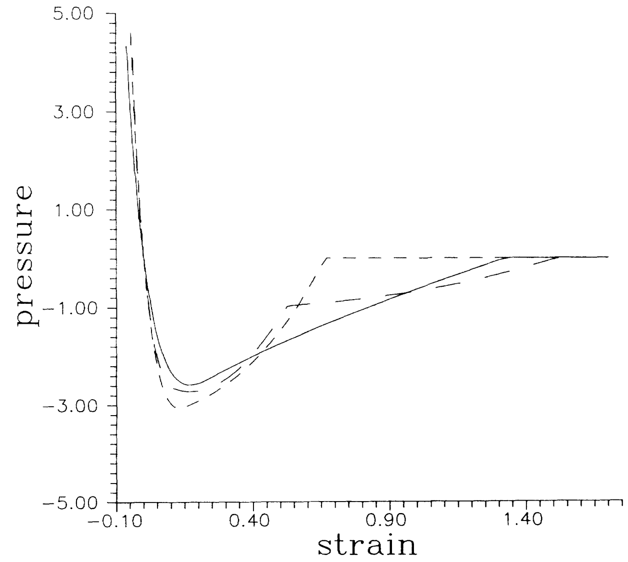

FIG. 11. Pressure vs strain for a $T=0$ LJ triangular lattice under ——, dilation; — — —, planar extension orthogonal to a lattice vector; and ---, planar extension along a lattice vector.

ments and results of Grady's analysis and compare with our adiabatic yield computer experiments. This represents an extension of the original application of the theory, which was to materials possessing heterogeneous nucleation sites such that the minimum energy path could be followed, to our perfect two-dimensional lattices, which require homogeneous nucleation sites for crack and void formation. Thus, this does not constitute a true test of the theory, but rather a test of its applicability to our materials and experiments.

The theoretical strength of the material, as an upper bound to the material's spall strength, is taken to be the extremum in the cold pressure versus volume curve. A good estimate of this is given by

$$P^{\mathrm{th}}=(\tfrac{1}{8}\rho_0 U_{\mathrm{coh}} B_0)^{1/2} , \tag{16}$$

where P^{th} is the theoretical spall strength in terms of the zero-temperature cohesive energy U_{coh}, bulk modulus B_0, and density ρ_0. Values for the two potentials studied are given in Table II.

The characteristic length scale over which spallation occurs is set by the communication horizon. Events cannot transmit information faster than the sound speed of the material c_0. Thus, for a given time t the characteristic length scale s is

$$s \le 2c_0 t . \tag{17}$$

Here t is the time since initiation of tensile loading. The mean tension is the sample is then assumed to be a linear function of the product of time and strain rate as

$$P=B_0\dot{\epsilon}t . \tag{18}$$

Brittle failure occurs when the energy density input to the material $\int P\,d\epsilon$ equals the energy dissipated in brittle cracking per unit volume, as characterized by the fracture toughness K_c. The surface energy per unit volume created by opening a crack of characteristic size s is

$$\frac{3K_c^2}{B_0 s} . \tag{19}$$

Equating these terms results in an energy criterion leading to the following equation for the minimum spall strength via brittle cracking:

$$P^B=(3\rho c_0 K_c^2\dot{\epsilon})^{1/3} . \tag{20}$$

A demonstrated by Grady [12], the kinetic energy available for fracture is small compared to the elastic energy and consequently is neglected in the above.

Ductile failure arises from spherical cavitation through homogeneous nucleation that is driven by plastic flow. When a critical void volume fraction ϕ_c is reached, the material can no longer support the tensile stress. The work required to create the voids is characterized by the plastic flow stress Y times this critical void fraction. As before, by balancing this against the energy stored in the material by the tensile stress and again neglecting the kinetic-energy term, the minimum spall strength for ductile failure becomes

$$P^D=(2\rho c_0^2 Y\phi_c)^{1/2} . \tag{21}$$

Notice that it is not an explicit function of the strain rate.

Although the brittle fracture toughness and the plastic flow stress are engineering material properties that can be determined through suitable experiments, some definition must be used to extract them from our computer simulations. An estimate of the fracture toughness can be obtained from the Griffith crack model, yielding

$$K_c^2=2\gamma E , \tag{22}$$

where γ is the surface tension. This can be estimated for our materials in terms of the cohesive energy of the potential divided by the surface area occupied per atom $\gamma\approx\varepsilon/\sigma^2$. The plastic flow stress is usually defined in terms of the onset of creep, occurring at some small strain, typically $Y\approx G/20\approx E/60$. Finally, the critical void fraction can be taken as 15%, where the linear distance between the voids is approximately the diameter of the voids. Though these estimates are crude, they are typical of the approximations used in defining them in the engineering sense and will suffice to illustrate the trends in this theory. Predictions for the three types of failure are given in Table II.

The results of the adiabatic tensile tests are plotted against the predictions of Grady's analysis in Fig. 12. Here it is seen that the range of strain rate probed covers the expected transition from brittle to ductile failure for both potentials. The spall strength of the EAM model material demonstrates linear behavior with $\log_{10}\dot{\epsilon}$. The magnitude of the predicted spall strength is within the error of the above approximations. However, the simulation data do not show the predicted abrupt transition from brittle to ductile spallation. The LJ material exhibits a similar behavior over the range studied, with spall strength growing linearly with $\log_{10}\dot{\epsilon}$, although significantly higher in magnitude than for the EAM potential. The measured spall strength does not reflect the trends in the predictions, and further, lies below the plastic criterion. However, as the true plastic flow strength is

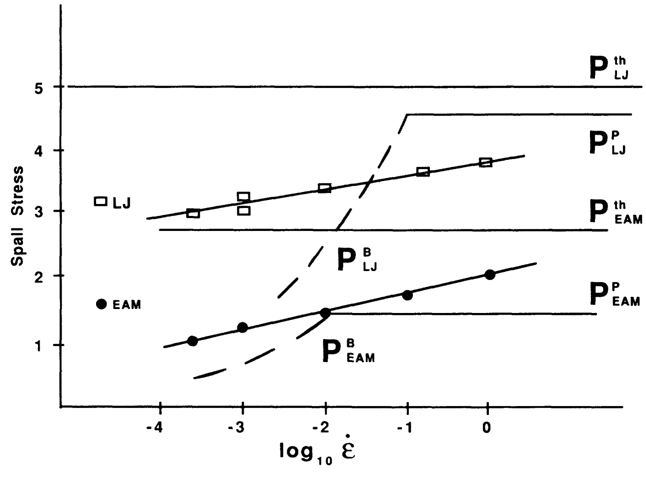

FIG. 12. Comparison of the energy-based spall criteria P^{th} (——), P^D (——), P^B (--), and the computer simulations ($T=0.17$): (a) EAM (○); (b) LJ (□), with best-fit lines.

expected to be an increasing function of the strain rate, there might be better agreement if strain rate effects are taken into account.

Grady also noted that experimental measurements do not show the abrupt transition from brittle to plastic spallation, and proposed a smooth transition regime where both mechanisms are important. Based on our approximations and using our material properties, Fig. 2 in his paper [11] would indicate that this transition region should be very small. In conclusion, the extended application of this minimum-energy criterion to perfect materials, where homogeneous nucleation of voids and cracks is required, results in poor predictions for the spall strength.

The communication horizon limits the range of accessible shear rates for the simulations. The characteristic distance s describing the scale over which spallation occurs must be less than the size of the simulation cell. Otherwise, a crack that spans the simulation cell will induce failure even though the energy criterion states that it is stable. The mathematical analysis results in the following formula for the communication horizon for ductile failure:

$$s=\left[\frac{8Y\phi_C}{\rho\dot{\epsilon}_0^2}\right]^{1/2}, \tag{23}$$

and for brittle fracture

$$s=2\left[\frac{\sqrt{3}K_c}{\rho c_0\dot{\epsilon}_0}\right]^{2/3}. \tag{24}$$

Figure 13 demonstrates the spall size expected for both mechanisms and potentials. The brittle failure size is the same for both potentials since the fracture toughness is proportional to the square root of the modulus, or in other words, proportional to c_0. Above $\dot{\epsilon}=1$, the ductile void size becomes smaller than the spacing between atoms, which clearly violates the macroscopic analysis. Below $\dot{\epsilon}=10^{-4}$ the critical crack size exceeds 1000 interaction lengths, thus requiring two-dimensional simulations in excess of 10^6 atoms, our current capability. All of our results fall within this range, and qualitatively follow this trend. At shear rates of order 1 the material failed without generating voids or cracks. Reducing the shear rate resulted in increasing void or crack size before mechanical failure. For the LJ potential we extracted an estimate of this size from the plots shown above (Fig. 10). The size s was defined as the average horizontal (x) distance between cracks or voids, which correlated well with the characteristic crack length of the material near failure. As seen in Fig. 13, our measured lengths in units of σ are distinctly lower than the theoretical estimates for the LJ potential. The points lie along a line with slope closer to the $-\frac{2}{3}$ slope predicted for brittle fracture than the -1 slope for ductile failure.

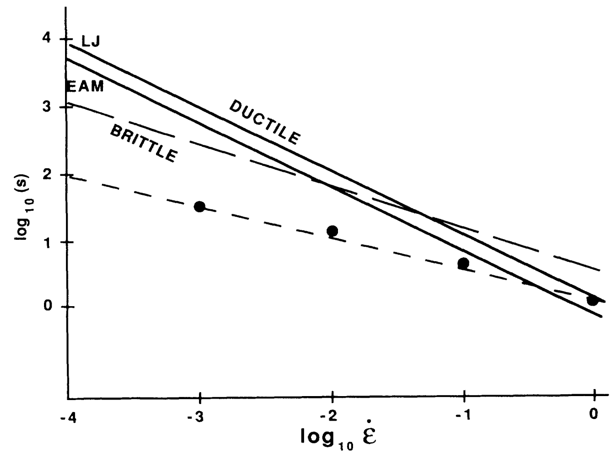

FIG. 13. Comparison of spall fragment size vs strain rate. ○, simulation results; ---, $-\frac{1}{2}$ power-law fit, energy-criterion-based theory for ductile failure (two lines as marked for LJ and EAM model), brittle failure (— — —, the same for both potentials).

B. Dislocation-dynamics limited failure

To explain the scaling of spall strength with strain rate, a dislocation dynamics model is presented. This phenomenological model relates the activation energy for dislocation nucleation and motion to the imposed stress. A criterion for plastic flow leading to spallation is invoked, relating the strain rate to the plastic strain. The result is an equation relating spall strength to strain rate in terms of the elastic constants of the material that not only captures the form of the correlation observed above, but is also reasonably quantitative. A number of previous investigations of fracture have used the stress as an internal variable to describe the nonequilibrium system Hamiltonian, but usually with the further assumption of local thermodynamic equilibrium [1,7,13]. Here, the system is far from thermodynamic equilibrium at fracture and rate effects are important.

The key criterion for spallation in this experiment where the external strain rate is imposed on the system is postulated to be

$$\dot{\epsilon}_p\approx\dot{\epsilon}\ . \tag{25}$$

When the plastic strain rate equals the imposed strain rate the material flows and can no longer support stresses. Further, once the material begins to fail in our experiments the stored elastic energy can be relieved and the material spalls.

The plastic strain rate is the product of three terms

$$\dot{\epsilon}_p=bNv\ , \tag{26}$$

the magnitude of the Burgers vector b (representing the amount of displacement carried per dislocation), the dislocation number density N, and the dislocation velocity v. Both the dislocation number density and the dislocation velocity in our perfect crystal will be taken to be activated processes. It is supposed that the key internal variable describing the free energy of the system is the stress. Nucleation must be homogeneous in our perfect crystal and will be an activated process. Extrapolation of these results to three dimensions, where dislocations have a more complex character, requires further development.

Following ideas latent in Ladd's article [14], we parametrize the free energy of a two-dimensional dislocation (minus the core part, which drops out of our analysis) as

$$E_D \approx Db^2, \quad D = \frac{BG}{\pi(B+G)} \ . \tag{27}$$

This relation for D is derived through elasticity theory and will suffice to give the scaling necessary for our analysis.

For homogeneous nucleation the major effect of an imposed stress τ will be to lower the energy penalty associated with dislocation formation. The elastic work done on the sample is a measure of this lowering, representing the straining of the lattice and the stretching of the atoms out of their potential minima. Thus, the free energy per atom associated with homogeneous nucleation of a dislocation will be

$$E_n \approx E_D - \tau\epsilon_e/\rho \ , \tag{28}$$

with ϵ_e the elastic strain. Homogeneous nucleation is known to be important only in perfect crystals at very high stress levels (greater than or equal to 10% of the shear modulus), which is the regime of our experiments. Although nucleation kinetics must play a role at short times and high strain rates, it is beyond the scope of this model to properly account for kinetic effects. We will simply assume that the nucleation density is in equilibrium with the applied stress level.

The force acting on a dislocation is proportional to τb. Thus, the energy required to move a distance l in the material is given by τbl. As this energy is available due to the imposed strain, the activation energy required for dislocation motion is lowered by this amount. Such activated dislocation movement is given in standard developments, such as Ref. [1], as

$$v = v_0 e^{-E_v/k_B T}, \quad E_v \approx E_D - \tau bl \ . \tag{29}$$

In both the above equations for the activated processes, scaling relations are invoked at the state of spallation. Other factors that are not strong functions of the state of the material at spallation will divide out in what follows. Again, arguments of this character have been previously invoked to explain the plastic shear flow of materials [7].

Two modeling assumptions are made that simplify the analysis but limit the applicability of the results. It is assumed that the system is being examined about a reference state, which is the limit of strain rates equal to the vibrational frequency of the atoms $\dot{\epsilon}_0 = 1$ characterized by *spall stress* τ_0. Near this state, it will be assumed that both the characteristic length of the dislocation motion l and the amount of elastic strain per atom ϵ/ρ are not strong functions of the imposed strain rate, both reasonable for these experiments. Further, the equilibrium values of the elastic and material constants will be used for the dislocation energy. The unknown terms, the dislocation hop length and the elastic strain, can then be determined by scaling the free-energy contributions from the imposed strain to the nucleation and dislocation velocity to that of dislocation creation. This states that at the reference state the stress at spallation is comparable to the dominant activation energies for nucleation and dislocation motion, resulting in

$$l = \frac{Db}{\tau_0} \ , \tag{30}$$

$$\epsilon_e/\rho = \alpha \frac{Db^2}{\tau_0} \ . \tag{31}$$

The value of the dislocation motion distance per jump l is approximately equal to b, as expected for two-dimensional lattices. However, because D is comparable to or greater than τ_0, the proportionality constant α must be $\approx 10\%$ such that the elastic strain $\epsilon_e \lesssim 10\%$ at failure, as observed. Thus, the scaling relations taken above can be made numerically consistent with known behavior through the introduction of only one parameter, which will have only minor effects on the quantitative spallation predictions.

Combining the above relations and taking the ratio of the strain rate to that at the reference state ($\dot{\epsilon}_0$) results in

$$\tau - \tau_0 = \left[\frac{\tau_0 k_B T}{(1+\alpha) b^2 D} \right] \ln \frac{\dot{\epsilon}}{\dot{\epsilon}_0} \ . \tag{32}$$

This relationship justifies the form of the empirically observed linearity between spall stress and the logarithm of the strain rate and as such can be directly compared to the simulation results. The value of $\alpha = 0.1$ was taken as an upper bound from the simulation results (see Fig. 9). Table III compares the slopes measured in Fig. 12 with the coefficient in our phenomenological model, where τ_0 was extracted from the fit and a value of $b = 2^{1/6}$ was used as an estimate of the magnitude of the Burgers vector. The agreement between the predicted and measured slopes, both based on the measured value of the spall stress τ_0, is good. The expected temperature dependence, which is linear with T (the elastic constants are only weakly dependent on temperature), is less than that predicted by Eq. (32). This relation can be used to generate a master plot for the computer data, as shown in Fig. 14. Dividing the spall stress by the reference spall stress and multiplying by the ratio of the dislocation energy parameter D to the temperature normalizes the stress for the different conditions and materials. Although the temperature dependence is not entirely accurate, this normalization does correct for the differences in material properties.

We can also estimate the scaling of spall fragment size with strain rate from the dislocation nucleation density. To first order, the distance between dislocations will be

$$s \propto 1/\sqrt{N} \approx 1/(N_0 e^{-E_D/k_B T} e^{(\tau_s \epsilon_e/\rho)/k_B T})^{1/2} \ . \tag{33}$$

Substituting the spall stress from Eq. (32) and elastic

TABLE III. Comparison of failure curves.

Model	Temp.	τ_0 meas.	Slope meas.	Slope Eq. (32)	Slope Eq. (36)	τ_0 Eq. (36)
EAM	0.17	2.05	0.124	0.16	0.06	1.4
EAM	0.075	2.16	0.078	0.081	0.03	1.4
LJ	0.17	3.65	0.079	0.13	0.06	3.4
LJ	0.075	3.80	0.049	0.046	0.03	3.4

strain ϵ_e from Eq. (31) into the above results in

$$s \approx \dot{\epsilon}^{-1/2} . \tag{34}$$

This is the scaling observed in our simulations (see Fig. 13), and serves as a consistency check of our proposed model.

This model is consistent with previous simulation work on measuring shear stress under high rates of shear strain. Hoover, Ladd, and Moran [15] show data that were later fitted by Ladd [14]:

$$\tau_{xy}=\tau_{xy,0}(\dot{\epsilon}_{xy}/\dot{\epsilon}_{xy,0})^{\gamma(T)}, \quad \gamma(T)=\frac{3k_BT}{Db^2} . \tag{35}$$

For small differences from the reference state, taking the logarithm of both sides and expanding the term for the stress ratio demonstrates that the empirical fit of Ladd is equivalent to our phenomenological model (except for a simple numerical factor) in this limit. We refitted their data to our model and found almost equivalent agreement to the published plots. The temperature dependence of our data does not follow the expected linear dependence of the coefficient (when material properties are assumed to be constant), but is weaker. However, the range in shear stress covered in their data is significantly greater than that to which our analysis is applicable.

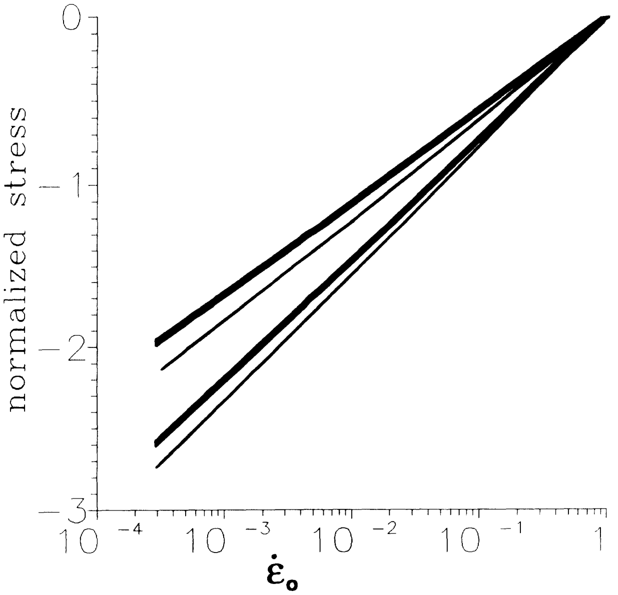

FIG. 14. Normalized spall stress $[(\tau-\tau_0)/\tau_0](D/T)$ vs $\dot{\epsilon}$ on a logarithmic scale, based on Eq. (32). EAM (heavy lines), LJ (light lines), $T=0.075$ (lower pair of curves), $T=0.17$ (upper pair).

As stated above, incorporation of a strain rate dependence in the plastic flow stress Y would improve the predictions of Grady's energy-based criterion for ductile failure for our systems. Assuming that activated dislocation motion would reduce the plastic flow stress for materials under tension, τ from formula (32) above is substituted for Y in the spall criterion for ductile failure, Eq. (21). The result, after expanding the square root, is

$$P^D=(2\rho c_0^2 Y_0 \phi_c)^{1/2}\left[1+\frac{k_BT}{2(1+\alpha)b^2D}\ln\frac{\dot{\epsilon}}{\dot{\epsilon}_0}\right] . \tag{36}$$

Thus, we see that invoking the same argument concerning ductile fracture improves the correspondence of Grady's analysis. Further, the above formula relates the high strain rate limiting spall strength τ_0 to the limiting ductile shear stress Y_0 and the critical void fraction ϕ_c. The predictions for the magnitude of τ_0 are lower than observed but reasonable. However, the ratio of the predicted slopes for the two materials, a more sensitive test, is incorrect. Note that this result is dependent upon our choice of plastic flow strength Y_0. The ratio of τ_0 for our two materials does not scale as predicted by the equation above, but rather scales in accordance with the theoretical strength of the material, Eq. (16).

The observation from Grady's comparison to experimental data, that there is no sharp transition from brittle to plastic spall as the strain rate is increased, follows from a model based on dislocation dynamics. Empirical fits to slow crack propagation have a similar form as above; the time to failure goes exponentially with the stress ([1], p. 154, Eq. 465). Thus, since the time is given by the strain divided by the strain rate and the total strain to failure is relatively constant, the measured stress at failure will increase with the log of the strain rate. Consequently, the dependence of stress on strain does not change functional form between low strain, crack-dominated failure to plastic flow limited failure at high strain.

C. Analysis of spallation simulations

With the above model experiments, some of the important behavior of the spallation simulations can be explained. As noted above, the reflection of the initial shock waves off the free surfaces generates a family of release waves, which spread as they propagate through the material. The width of this zone δx controls the strain rate at the spall plane. This phenomenon is understood to be a direct result of inelastic material behavior [16] and can be estimated as

$$\frac{\delta x}{L_x}=\left[\frac{B_1-1}{8}\right]\left[\frac{P_s}{B_0}\right], \quad B(P)=B_0+B_1P , \tag{37}$$

where P_s is the pressure at the release front and L_x is the characteristic length of the material. This relation is derived by using the Murnagan equation of state and calculating the position of maximum stress when the zero-stress condition is realized at the spall plane after the release waves have initially collided. Since the pressure rise will be proportional to the particle velocity times the sound velocity (Rankie-Hugoniot equations) $P_x \approx \rho U_p U_s$, with U_s the shock velocity, the zone width becomes

$$\frac{\delta x}{L_x} = \frac{(B_1 - 1)}{8} \frac{U_p U_s}{c_0^2} , \tag{38}$$

showing how the zone increases with increasing particle velocity and decreases with increasing sound velocity. The material property B_1 has been measured as ≈ 4.7 for the EAM and ≈ 6.5 for the LJ materials studied.

The effective strain rate is then estimated by the initial particle velocity divided by the zone width

$$\dot{\epsilon} \approx \frac{U_p}{\delta_x} . \tag{39}$$

The maximum stress available for fracturing our material is estimated from elastic wave mechanics as

$$\begin{gathered} \sigma' = (B+G)\epsilon_{xx}, \quad \epsilon_{xx} \approx \dot{\epsilon}_{xx} t , \\ t \approx \delta_x / U_s \quad \epsilon_{xx} \approx U_p / U_s . \end{gathered} \tag{40}$$

These relations result in the maximum strain and stress in the spallation zone, which can be used to estimate whether or not spallation occurs. The results will be upper bounds on the strain and stress values, since the use of U_p for the relative particle velocity of the release waves is clearly an overestimate if any energy is lost during wave propagation, and the use of linear elasticity will also overestimate the resultant stress. As shown in Table IV, these results predict the gross features of the observed behavior. Namely, for the EAM material, the maximum strain at the spall plane of 10% and the maximum stress of 160% of the spall strength predict the observed spallation. For the LJ material the predicted strain of 6% is less than that needed to spall and the stress at the spall plane is just comparable to the spall strength. Hence, we would predict that the LJ material should be damaged but not totally spalled, as observed. Given the weak dependence of spall strength on strain rate, the major effects of changing from the EAM to the LJ potential are to increase the spall strength and lower the total strain at the spall plane. The scaling arguments demonstrate qualitative trends and give reasonable first estimates.

V. CONCLUSIONS

This simulation work on model two-dimensional metals has provided information on the very high-strain-rate behavior during spallation. An actual impact experimental geometry has been simulated in two dimensions and the relevant physics extracted through model adiabatic expansion simulations. The adiabatic expansion experiments provide spall strength versus strain rate data for both the pairwise additive Lennard-Jones potential and the model-embedded-atom many-body potential. Although the macroscopic behavior was similar, the EAM material at failure exhibited ductilelike hole formation while the LJ material formed brittle cracks.

The results for the failure stress and void or crack size are explained within an activated dislocation motion model, such that the spall stress is predicted to grow as the logarithm of the strain rate. Quantitative estimates obtained from the scaling arguments are in reasonable comparison with the observed measurements. The reference state for these experiments is taken to be a strain rate on the order of the molecular vibration frequency, such that the material's theoretical strength is overcome. The functional form of this relationship is similar to that observed for slow crack propagation at low-strain rates, and so the experimental observation of continuous transition in spall stress in metals from brittle to plastic failure regimes is also suggested. Important differences in interpretation are expected for three-dimensional materials where dislocations and dislocation motion are richer and more complex in character.

Energy-based spall criteria were found not to predict the observed behavior very well, probably due to the importance of homogeneous nucleation in our perfect materials. The concept of a communication horizon is shown to be important in determining the validity of the simulated failure and the applicability of continuum theories. However, according to the scaling arguments for dislocation dynamics, the spall size is governed by the homogeneous nucleation density. The former analysis demonstrates the necessity of studying very large numbers of atoms for low strain rates, requiring the use of massively parallel computers and pushing the limits of current computational technology.

Simulations of spallation upon target impact demonstrate that the molecular behavior averages to the hydrodynamic predictions. At the simulated impact velocities inelastic material behavior creates a spallation zone with the spall plane defined by sharp shock predictions. Material failure is characterized by the opening of small voids that coalesce into cracks. Significant plastic flow is observed and most of the irreversible work goes into defect formation. Simple scaling laws demonstrate that the spall stress versus strain rate from the adiabatic expan-

TABLE IV. Model for spallation.

Experiment	$\dot{\epsilon}$ (est.)	$\dot{\epsilon}$ (meas.)	ϵ	$B+G$	σ'_{xx}	σ_{spall}
A (EAM)	0.06	0.01	0.1	27.3	2.9	1.8
B (LJ)	0.05	0.04	0.06	62.7	3.7	3.5

sion experiments explains the observed behavior. Essentially, in the regime explored, the ratio of the impact velocity to the material sound speed is important in determining spallation. However, we did not observe any quantitative difference in the amount of inelastic work done on the samples, as characterized by the change in the total kinetic energy. Further, when comparing the two model potentials, most of the behavior at high strain rates scaled with the equilibrium material properties. Other qualitative observations of the effects of polycrystallinity are suggestive of previous experimental observations and will be investigated further. Planned future work includes extension to three dimensions, where we expect qualitative differences due to the more complex nature of the defect structure.

ACKNOWLEDGMENTS

We would like to thank E. Cort of LANL for encouragement, support, and useful discussions concerning this work. The help of T. Dontje from TMC and J. Hammerberg, R. Ravelo, and S-P. Chen of LANL is gratefully acknowledged. We appreciate helpful comments on the manuscript from D. Grady of SNLA. N.J.W. acknowledges support from LANL and NSF. The computational resources were provided by the Advanced Computational Laboratory of Los Alamos National Laboratory.

---

[*] Present address: Department of Chemical Engineering, University of Delaware, Newark, DE 19716.

[1] A. Kelly and N. H. Macmillan, *Strong Solids* (Clarendon, Oxford, 1986).

[2] *Mechanical Properties at High Rates of Strain, 1984,* edited by J. Harding (Institute of Physics, Bristol, 1984), Vol. 70.

[3] P. S. Follansbee, in *Shock Waves in Condensed Matter, 1987,* edited by S. C. Schmidt and N. C. Holmes (Elsevier Science, Amsterdam, 1988), p. 249.

[4] B. L. Holian, A. F. Voter, N. J. Wagner, R. J. Ravelo, S. P. Chen, W. G. Hoover, C. G. Hoover, J. E. Hammerberg, and T. D. Dontje, Phys. Rev. A **43**, 2655 (1991).

[5] M. P. Allen and D. J. Tilsedey, *Computer Simulation of Liquids,* 2nd ed. (Clarendon, Oxford, 1989).

[6] B. L. Holian, in *Shock Waves in Condensed Matter, 1987* (Ref. [3]), p. 185.

[7] J. J. Gilman, Appl. Mech. Rev. **21**(8), 767 (1968).

[8] B. L. Holian, Phys. Rev. A **37**, 2562 (1988).

[9] D. G. Brandon, M. Boas, and Z. Rosenberg, in *Mechanical Properties at High Rates of Strain, 1984* (Ref. [2]), p. 261.

[10] B. L. Holian and D. E. Grady, in Phys. Rev. Lett. **60**, 1355 (1988).

[11] D. E. Grady, *Shock Waves in Condensed Matter, 1987* (Ref. [3]), p. 327.

[12] D. E. Grady, J. Mech. Phys. Sol. **36**, 353 (1988).

[13] R. L. Blumberg Selinger, Z-G. Wang, W. M. Gelbart, and A. Ben-Shaul, Phys. Rev. A **43**, 4396 (1991).

[14] A. J. C. Ladd, in *Shock Waves in Condensed Matter, 1985,* edited by S. C. Schmidt and N. C. Holmes (Plenum, New York, 1986), p. 267.

[15] W. G. Hoover, A. J. C. Ladd, and B. Moran, Phys. Rev. Lett. **48**, 1818 (1982).

[16] A. A. Keribas and I. D. Zakharenko, in *Mechanical Properties at High Rates of Strain, 1984* (Ref. [2]), p. 277.

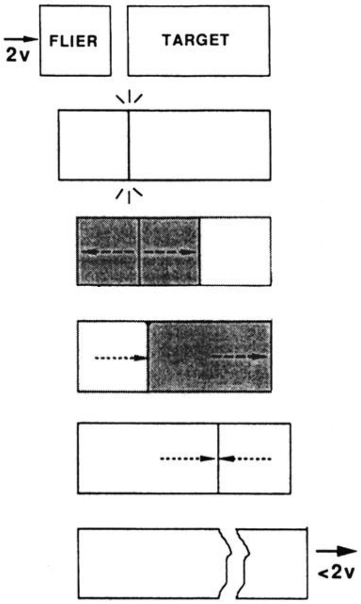

FIG. 1. Spallation experiment geometry.